COMMUNICATIONS CHEMISTRY

ARTICLE

DOI: 10.1038/s42004-018-0084-1 OPEN

Dandelion-shaped manganese sulfide in ether-based electrolyte for enhanced performance sodium-ion batteries

Duong Tung Pham[1], Balaji Sambandam[1], Sungjin Kim[1], Jeonggeun Jo[1], Seokhun Kim[1], Sohyun Park[1], Vinod Mathew[1], Yang-Kook Sun[2], Kwangho Kim[3,4] & Jaekook Kim[1]

Metal sulfide materials serve as environment-friendly, sustainable, and effective electrode materials for green-energy storage systems. However, their capacity-fading issues related to low electrical conductivity and drastic volume changes during electrochemical cycling have generally limited their application to sodium ion batteries. Here we show that with the combination of an ether-based $NaPF_6$/diglyme electrolyte, the dandelion-shaped manganese sulfide electrode displays enhanced reversible capacity, cycle life, and rate capability. The capacity of 340 mAh g^{-1} is maintained over more than 1000 cycles at a current density of 5.0 A g^{-1}. Furthermore, discharge capacities of 277 and 230 mAh g^{-1} at 10 and 20 A g^{-1} current densities, respectively, are obtained. Our work demonstrates the formation of a protective solid electrolyte interface layer along the surface of the primary seed particle that limits polysulfide dissolution and hence the preservation of the active material during reaction with sodium.

[1] Department of Materials Science and Engineering, Chonnam National University, Gwangju 500-757, South Korea. [2] Department of Energy Engineering, Hanyang University, Seoul 133-791, South Korea. [3] Global Frontier Center for Hybrid Interface Materials, Pusan National University, Busan 609-735, South Korea. [4] School of Materials Science and Engineering, Pusan National University, Busan 609-735, South Korea. Correspondence and requests for materials should be addressed to J.K. (email: jaekook@chonnam.ac.kr)

The revolution in the field of rechargeable battery technologies, specially, lithium ion batteries (LIBs) has made a significant contribution to the portable electronic market in our society. The ultimate goal is to realize the complete replacement of fossil fuels utilized for large-scale stationary and transport applications with green-energy sources. Considering that the exhaustion of fossil-based resources in the next few decades have been predicted, the LIB technology that store/release energy via chemical intercalation/de-intercalation of ions are being intensely investigated to power large-scale energy storage systems (ESSs) and vehicular applications[1,2]. However, the energy density and cycle life delivered by the current LIBs still remain inadequate for long vehicle or large-scale ESSs[3]. As a promising replacement for lithium, sodium-ion batteries (SIBs) have emerged due to the low-cost and abundance of sodium in the earth's crust[4–8]. However, SIBs undergo capacity fading because of the limited ion-mobility and structural expansion or morphological disorder issues related to the larger ionic radius of Na^+ (1.06 Å) compared to Li^+ (0.76 Å)[9]. Thus, the performance of SIBs are still far from the expectations, and the understanding of Na-based materials is much less than that of their Li-based counterparts[10]. In order to explore the utilization of SIBs for practical ESSs applications, promoting low-cost pros and compensating low-performance cons through new approaches are vitally important to realize high capacity, long cycle life, and superior rate performance in SIBs[11,12].

As a priority mission for the ESSs design, high energy density materials with long-term development, low investment cost, and environmental friendliness are preferred. From this point of view, transition metal sulfides containing S^{2-}/S_2^{2-} dimers have attracted tremendous attention for ESSs because of their unique properties of high energy density, good conductivity and excellent stability[13]. In addition, the huge resource of sulfide materials in natural mines offers scalable, low-cost, and sustainable SIB anodes. Therefore, the investigations on the sulfide family members, such as FeS_2[14], CoS[15], MoS_2[16], and Cu_xS[17,18], for SIBs were recently reported. Similar to other SIB anodes, sulfides experience the problems of structural degradation upon repeated Na^+ ion insertion/extraction due to sudden large volume change, causing detrimentally impact to the cycle life[19]. Moreover, the reaction mechanism involving the conversion of MS/Na to Na_2S/Na ($MS + Na \rightarrow Na_2S + M$) after the first discharge cycle, and the dissolution of polysulfide (S_n) are considered to be the most challenging issues that limit the practical application of sulfide anodes in SIBs[20]. Focusing on the usual strategy of enhancing electrochemical performance, many research groups aggressively used in situ synthesis to prepare composites based on sulfides and electrically conductive carbon additives. Reduced graphene oxide (RGO) and carbon nanotube (CNT) are the outstanding carbon source selections in this regard because of their high electrical conductivity, stable mechanical strengths, and superior surface areas. Therefore, several modifications of growing RGO/CNT in situ within sulfides were successfully synthesized, and gathered momentum in enhancing the performances of sulfides[21–23]. Although carbon-based addition improved the electrochemical properties of sulfide anodes in LIB/SIB applications, it is important to focus on fundamental issues such as material morphology or cell designation strategies that have far greater potential to be explored scientifically.

Emerging as a typical candidate alongside the sulfide materials, MnS has demonstrated enhanced and novel properties in diverse applications including optical and optoelectric devices. This materials also has an effective antiferromagnetic structure for magnetic application and is a promising electrode material for LIBs or supercapacitors[24–26]. Among the three polymorphs (α, β, and γ) of MnS, the stable layer rock–salt structure (α-MnS) has received much attention for its use in developing an effective ESS. Meanwhile, multiple efforts have been focused on producing stable nanostructures, such as nanobelts[27], octahedron submicrocrystals[26], and nanoparticle films[28], which are expected to improve the mechanical strength and reduce the diffusion path of Li^+ ions. However, unexpectedly, the electrochemical performance have shown capacity fade with short cycle life. A recent work highlighted the formation of a composite formed from hollow microsphere-type MnS particles and RGO sheets[29]. This smart MnS/RGO combination showed remarkable results, with specific capacities of 830 mAh g^{-1} attained at 0.5 A g^{-1} after 100 cycles and 308 mAh g^{-1} at 0.1 A g^{-1} after 125 cycles for LIB and SIB, respectively. Although some positive results were observed, the lack of clarity on the electrochemical mechanism has led to questions on the role of RGO in determining the overall performance.

In this work, the superior performance of DS-MnS (dandelion-shaped manganese sulfide) anode prepared by a solvothermal synthesis for sodium-ion battery applications is reported. The prepared electrode benefits from the advantages of a stable morphology with secondary structure built from primary nanosized seeds. The structural design of this material promotes mechanical stability in addition to facilitating a large active surface area, both arising from the presence of primary nanosized particles. Furthermore, the selection of an electrolyte component based on diglyme demonstrates an effective approach for realizing stable SIBs with long cycle life[16,29]. The prepared DS-MnS could achieve a high specific capacity and excellent rate capability with long cycle life.

Results

Structural and characterization of dandelion-shape MnS electrodes. The present MnS was successfully synthesized by the facile one-step solvothermal method. Figure 1a shows the XRD pattern of pristine MnS with high crystallinity that perfectly matched with the standard cubic phase (JCPDS 64-3438, space group: *Fm-3m*). The highly reducing function of $NaBH_4$ in a polyol medium was carefully investigated by Laliberte et al.[30] Therefore, in this research, a mixture of $NaBH_4$ with EG was selected as an excellent reduction agent for the sulfur powder. This process is called the sulfurated sodium borohydride process. Moreover, the high pH level of the mixture was favorable for sulfide metal formation[31]. Supplementary Figure 1 illustrates a possible reaction mechanism of the solvothermal process, wherein the layer-structured MnS could be easily formed because of the reducing agent polysulfide $BH_2S_3^-$. The solvothermal method was pursued to prepare the present MnS taking into view the successful features of this synthetic technique both from the academic and industrial perspectives. In general, the solvothermal method is a simple and efficient process utilizing cost-effective precursors performed under low initial reaction temperatures at equilibrium pressure. The liquid medium used in this method serves two different functions of not only playing the role of a solvent but also as a pressure transmitting medium. Further, this technique provides great flexibility to tune the properties, morphology, size, and structure of nanomaterials by simply varying the different reaction parameters, such as medium, precursors/additives and their concentrations, reaction time, temperature, pressure, pH, and filled volume of autoclave. The technique thus provides flexible in tuning reaction condition based on the liquid medium used at apparently low temperatures, ease of processing, and sample preparation. Moreover, this method can be suitable for the preparation of nanomaterials with different shapes/dimensions as compared to other methodologies[32].

The material surface morphology was investigated by SEM. Figure 1b illustrates the uniform distribution of spherical-shaped

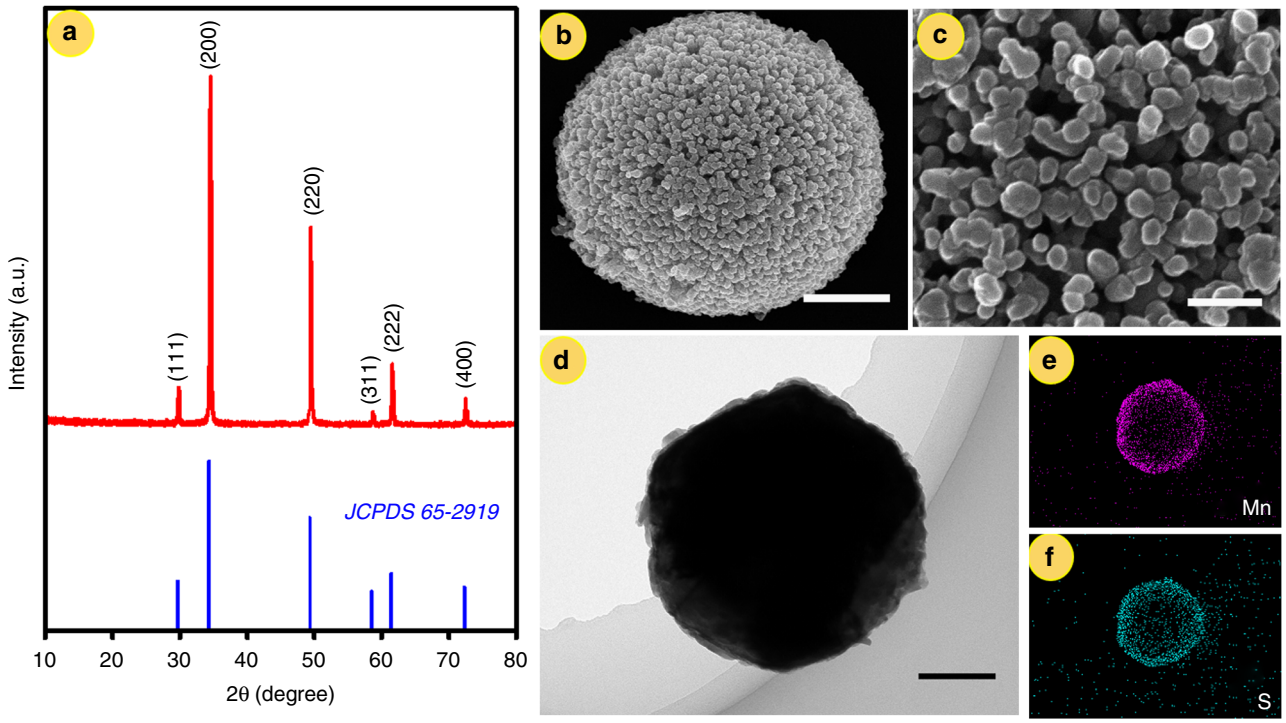

Fig. 1 Characterization of dandelion-shape MnS powder. **a** Synchrotron X-ray diffraction (SXRD) pattern of MnS (red line) with indexed crystal planes and JCPDS 65-2919 reference (blue line). **b**, **c** Low and high magnification FE-SEM images. Scale bar of **b** = 1 μm and **c** = 200 nm. **d**–**f** TEM image and elemental mapping of DS-MnS. Scale bar of **d** = 200 nm

dandelion particles of pristine MnS. Homogeneously distributed particles with average diameters of 50 nm are detected on the surface of the bulk particles, as evidenced from the magnified view of the dandelion surface in Fig. 1c. Moreover, these primary particles tend to grow outward with random arrangements and thereby create numerous spatial voids/pores that promote greater electrolyte wetting and hence more number of electrochemically active sites during reaction. TEM and EDS mapping images (Fig. 1d–f) clearly confirms the homogenous distribution of Mn and S elements in a secondary 3D MnS particle with spherical/dandelion-shaped morphology. Further, the evolution of the secondary morphology structure for the prepared MnS was investigated with respect to the reaction time and the results are provided in Supplementary Figure 2a–c. After 3 h reaction time, a mixed hexagonal and cubic phases of MnS is identified by XRD while the corresponding SEM image indicates the initial nucleation growth of secondary structure. However, after 6 h reaction, a pure MnS-cubic phase is obtained and the SEM study reveals the maturing of a spherical secondary morphology with imperfect primary particles exposed on the surface (Supplementary Figure 2b). Further, fully grown dandelion structures of the pure cubic MnS are observed after 12 h of reaction time.

Electrochemical performance of MnS/Na half-cell batteries. Figure 2a shows the CV curves of the DS-MnS electrode at a sweep rate of 0.2 mV s^{-1} in the 0–2.5 V potential range. Two wide irreversible peaks at 0.65 and 0.21 V observed in the first cathodic sweep can be assigned to the material interface intercalation, caused by the limitation of the reaction side along with the formation of a solid electrolyte interphase (SEI) layer. Besides, a group of corresponding peaks in the anodic sweep indicated multiple steps of the de-sodiation process. From the second cycle, new reduction peaks at 2.0, 1.56, 1.1 V represent Na^+ ion intercalation via several steps according to Eq. (1), and the conversion reaction described by Eq. (2) at 0.4 V peak[33,34]. In the next cycle, the cathodic peak at 0.4 V was gradually degenerated and replaced by a 0.8 V peak, indicating the decomposition of Na_xMnS into nanosized metallic Mn encapsulated by the Na_2S matrix. On the reverse sweep, broad peaks occurring between 1.5 V and 2.2 V are ascribed to the extraction of sodium ions and the oxidation of Mn metal to MnS, according to the unique conversion reaction described in Eq. (3)[35]:

$$MnS + xNa^+ + xe^- \rightarrow Na_xMnS \quad (x<2) \tag{1}$$

$$Na_x + MnS + (2-x)Na^+ + (2-x)e^- \rightarrow Na_2S + Mn \tag{2}$$

$$Na_2S + Mn - 2e^- - 2Na^+ \rightarrow MnS \tag{3}$$

Figure 2b depicts the selected electrochemical reaction profiles (1st, 2nd 50th and 150th cycles) of the prepared secondary MnS electrode in the working potential window of 0 to 2.5 V vs Na/Na^+ at the applied current density of 0.5 A g^{-1}. The first discharge capacity reached approximately 400 mAh g^{-1}, while the charge capacity ended at nearly 300 mAh g^{-1}. The low Coulombic efficiency of the first cycle (79%) may be caused by the SEI layer formation and other parasitic reactions including electrolyte decomposition. However, from the second cycle, the charge and discharge capacities are balanced, then gradually increases up to 430 mAh g^{-1} discharge capacity in the 150th cycle. Figure 2c represents an excellent cycling performance for more than 400 cycles with very little capacity decay (<2%). The activation process at 0.5 A g^{-1} needs more than 50 cycles as the number of active electrochemical sites increases on repeated Na^+ insertion/extraction at apparently low current densities[36]. Moreover, the long activation is probably caused by the breakdown of the bulk into nanosized seeds particles due to the repeated Na^+ insertion/

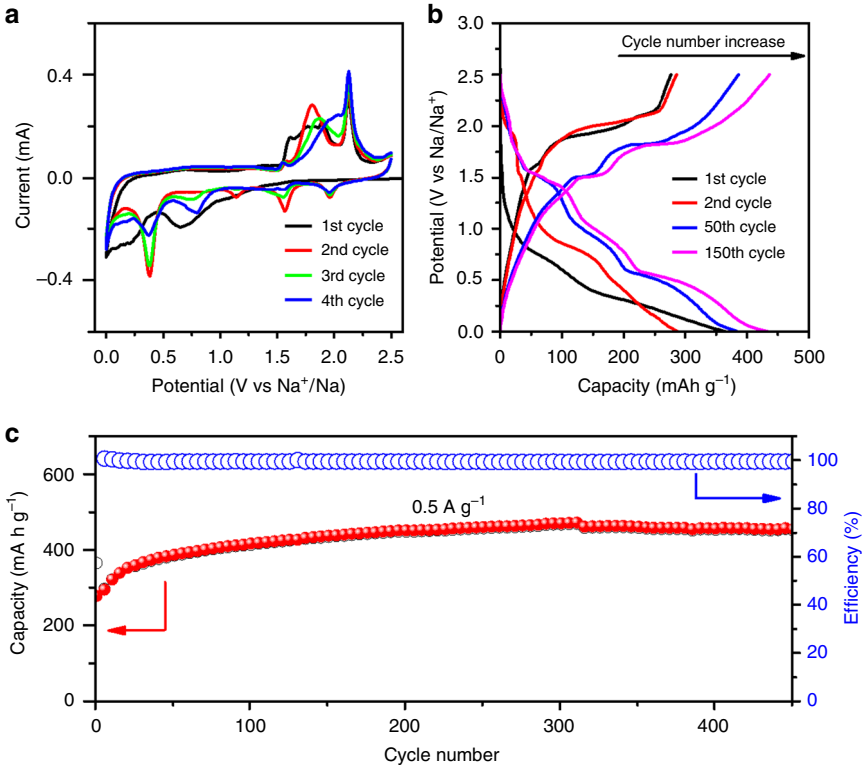

Fig. 2 Electrochemical performance of MnS/Na half-cell. **a** CV curves of DS-MnS from 0 to 2.5 V at a scan rate of 0.2 mV s^{-1}. **b** Galvanostatic charge/discharge curve at 0.5 A g^{-1} current drain. **c** The corresponding cycle performance at the same current drain. The red and blue scatters in **c** represent obtained capacity and corresponding columbic efficiency, respectively

extraction processes. At the end of 450 cycles, the present DS-MnS electrode displays a reversible capacity of 420 mAh g^{-1}. In order to understand the electrode morphology after electrochemical cycling, the ex situ SEM was recorded after a 50-cycle loading. The results (in Supplementary Figure 3a–d) clearly show that the dandelion-shaped morphology of the MnS electrode no longer exists after the activation process. Instead, the morphology reveals nano-scale particles of sizes within the 30 to 40 nm range probably arising from the pulverization of the secondary structure after Na^+ insertion/extraction processes. This pulverization effect during the electrode activation process is also confirmed from TEM studies, as observed from the fragmented particle morphology, in Fig. 3a, for the sample electrode at discharge state. Moreover, the elemental mapping studies conducted on a prescribed area (Fig. 3b) revealed that the Na and S elements are uniformly distributed, while the Mn element distribution is uneven concentrated only at specific regions under the area of study. Also the elemental line profile along the earmarked direction (blue arrow in Fig. 3b) reflects the high intensity of the Mn signal along the specific orientation that matches well with the mapping result. Nevertheless, the breakdown or collapse of the dandelion morphology to smaller nanoparticles leads to enhanced electrode/electrolyte contact area and hence Na^+ ion diffusion pathways leading to higher specific capacities during the initial few cycles, this being congruent with the initial electrode activation observed in Fig. 2c[33].

Correspondingly, noticeable changes of gradual deformation in the initial few galvanostatic charge/discharge curves occur along the activation period, as represented in Fig. 2b. In other words, the discharge plateaus at 2.0, 1.5, 1.0, and 0.5 V gradually appeared and extended, demonstrating the improvement of the sodium-ion exchange behavior caused by the increasing number of active electrochemical sites. Besides, the two charge plateaus at 1.5 and 1.8 V matched well with the observations from the CV studies. In addition, the observation of additional capacity after activation, at low working potential (below 0.2 V) could be related to the interfacial sodium-ion storage due to parasitic reactions[33]. In other words, the activation process increases the number of active sites as the dandelion-type secondary particles are broken into nanoparticles and thereby improve the Na^+ diffusion kinetics. In addition, the repeated sodiation can lead to excess Na^+ insertion into voids or crystal defects due to the collapse of the crystalline structure and generation of a large number of voids[29,33]. Furthermore, it is possible that the capacity contribution at very low working potentials can also arise from the parasitic reaction of Na-ion adsorption into the conductive carbon (10% in weight) that was used for electrode fabrication[37]. A low current density measurement can help in a detailed understanding of the electrochemical mechanism occurring in the present MnS electrode used in a diglyme-based electrolyte solution. Thus, the electrochemical profile obtained for the first cycle under a C/20 (~50 mA g^{-1}) current density (Supplementary Figure 4) can be separated into high discharge potential regions that are represented by intercalation reactions while the intermediate potential range is attributed to conversion reaction. Finally, the low discharge potentials correspond to parasitic reaction and the charge potentials are mostly defined by rapidly occurring conversion reaction. Furthermore, the detailed electrochemical profiles and the corresponding cycle performance at C/20 current density are included in Supplementary Figures 5a and b. The discharge/charge curves of the 1st, 2nd, 10th and 15th cycles are presented clearly illustrating the effect of side reactions to the Columbic efficiency. In the initial few cycles, average reversible specific capacities of ~500 mAh g^{-1} are registered while gradually increasing during the consecutive cycles. In addition to the activation process of the MnS electrode, a complex

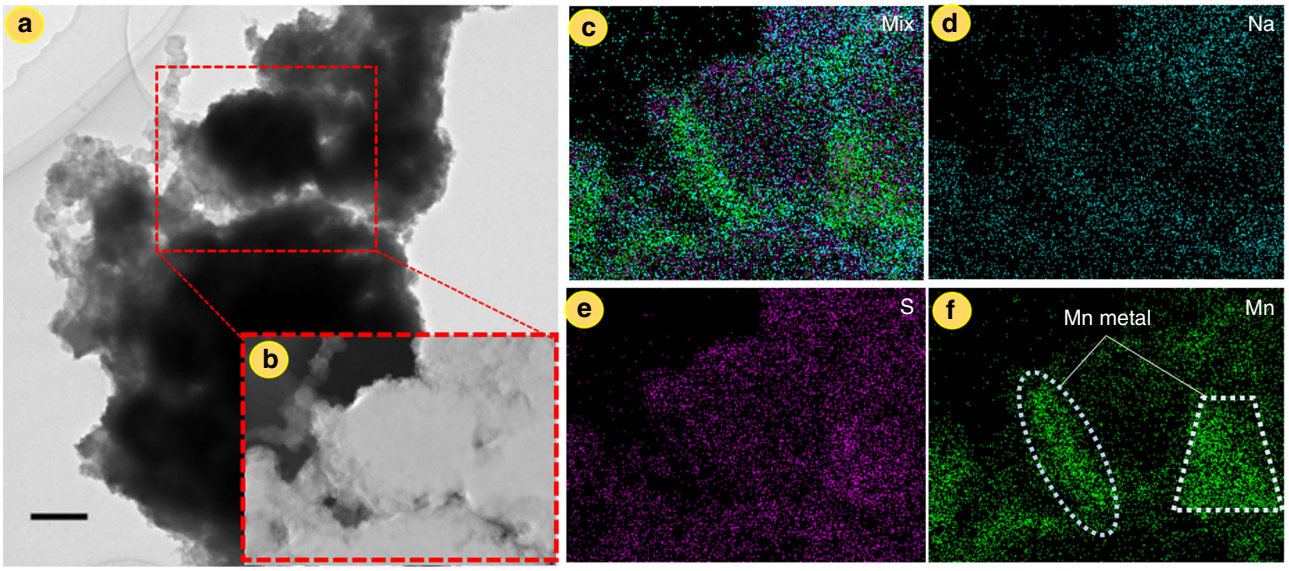

Fig. 3 Ex-situ TEM characterization. **a** High magnification image of discharge sample. Scale bar = 200 nm. **b** corresponding HAADF image of selected area (red box). **c**–**f** Mapping profiles for mixed state, and individual states of Na, S, and Mn elements. The marked areas in **f** depict the concentrated metallic Mn

electrochemical mechanism in combination with other parasitic reactions such as electrolyte decomposition, SEI layer formation and Na-ion adsorption by conductive carbon leads to the low charge capacity reversion in the first cycle. After that, the efficiency is quickly recovered and remains slightly fluctuated at ~100% during the subsequent cycles, indicating the cycling retention ability of the MnS electrode. The internal resistance variation related to the formation of the decomposition layer on the electrode between discharge/charge processes can cause slight irreversibility after the initial ten cycles and this phenomenon is discussed in detail in the section dealing with the analysis of the in situ PEIS results.

More importantly, the electrochemical profiles obtained for the present DS- MnS electrode used in combination with a unique diglyme-based electrolyte system are significantly different from those obtained for the already reported MnS electrodes utilizing the commonly used carbonate-based electrolytes for SIB applications[29]. A comparison of the electrochemical profiles for MnS electrodes (Supplementary Figures 6a and b) in the present glyme electrolyte and the conventional carbonate electrolyte (1 M $NaPF_6$ in EC/DMC (1:1) + 2%FEC), illustrates that the first discharge curves show insignificant variations, however, the following charge curves present striking differences. In specific, the MnS electrode in the diglyme-based electrolyte medium shows a unique plateau corresponding to ~100 mAh g^{-1} capacity at 2.0 V thus contributing to the overall higher charge capacity and lower irreversibility than the electrode utilizing the carbonate-based electrolyte[13]. As expected, the CV profiles (in Fig. 2a) reveal a corresponding dominant anodic peaks at 2 V as well as at 1.6 V. These features are the typical characteristics of similar high temperature α-MnS electrodes with cubic lattice reported for NIBs[38]. Concordantly, as expected, the related oxidation peaks of α-MnS electrode used in LIB applications are observed at slightly higher potentials (~2 and 2.5 V) and these features are attributed to the reformation of the MnS phase[33,39]. Nevertheless, these redox features are completely different from the only one oxidation peak (around 1.5 V) observed during the anodic scan of the low-temperature γ-MnS electrode with hexagonal lattice in a lithium half-cell configuration[40,41]. Similarly, it is reasonable to conclude that, in the present case, the 2 V feature in the CV and the charge profiles of the MnS electrode are related to the fast reformation of pristine MnS via conversion reaction (Eq. 3). However, the 2 V feature observed for the MnS electrode in diglyme-based electrolyte is more pronounced compared to the counterpart shoulder feature observed in a carbonate-based electrolyte solution (Supplementary Figure 6a). The unique feature can be related to the increased amount of polysulfide formed during sodiation in the diglyme-based electrolyte and the fast kinetic process of pristine MnS reformation due to the unique electrode nanostructure during de-sodiation. It is worth noting that more studies are required to further ascertain these conclusions.

Generally, the first discharge reaction of the MnS, which is represented by the phase separation reaction (i.e., $MnS + 2Na^+ + 2e^- \rightarrow Mn + Na_2S$), contributes to drastic volume variation and structural degradation of the electrode. The molar volume difference between initial and final phases (MnS and Na_2S) in the first discharge is estimated to be ~190% and the large volume change is induced by the uptake of high sodium content during the electrochemical discharge reaction[42]. Interestingly, upon repeated cycling, the (de-)intercalation process at high (charge) discharge potential regions can provide necessary padding-steps that tend to effectively reduce further drastic volume changes, as observed from the decent cycling performance presented in Fig. 2c. Nevertheless, suitable electrode designs are necessary to compensate for this long-term drawback. In addition, the high solubility of sodium polysulfide generated during cycling also affects the amount of active material and ultimately leads to rapid capacity fade of the MnS electrode[43]. Earlier investigations have concluded that polysulfides tend to show higher solubility in high nucleophilic solvents based on carbonates, esters, aldehydes, ketones, and anhydrides[44]. Such reactions lead to active material loss and thereby contribute to sudden capacity fade and poor electrode performances (Supplementary Figure 6b). In the present case, the higher irreversibility and lower charge capacity of the MnS electrode in the carbonate electrolyte medium can be related to the polysulfide dissolution and hence active material loss. For further understanding, the separators (Whatman glass fiber) recovered ex-situ from cycled half-cells utilizing glyme-based and carbonate-based electrolytes, respectively, were studied by SEM to observe morphology variations. The SEM images (Supplementary Figure 7a–c) clearly showed distinguishable changes in the morphologies of separators from both test cells after 50-cycle loading. The separator recovered from the cell using ether-based

diglyme electrolyte shows little/insignificant morphology variation. However, a slightly eroded/roughened morphology in addition to discrete dendritic particles are revealed for the separator obtained from the carbonate electrolyte-contained test cell. This observation supports the conclusion that more solvent decomposition with greater polysulfide dissolution by chemical reaction can contribute to the short circuit phenomena due to sodium dendrite formation in the latter cell. These drawbacks therefore could ultimately contribute to the serious capacity decay observed during the cycling of the MnS electrode utilizing carbonate-based electrolytes. On the other hand, the consistently long charge plateau clearly demonstrates the fast reversible kinetic transformation of Na_2S/Mn to the parent MnS electrode in the diglyme electrolyte medium. The formation of metallic Mn at complete discharge can be related to the uneven distribution observed in the mapping image of just the Mn element (Fig. 3b) and the increased Mn spike in the line profiling (Supplementary Figure 8a–c) of the ex situ MnS electrode. In specific, the increased Mn distribution at the core of the regions earmarked in the mapping image indicates that metallic Mn particles are encapsulated by the outer shells of Na_2S and this phenomenon is discussed later in the section. Galvanostatic intermittent titration (GITT) measurement was performed for the first discharge/charge cycle of the MnS/Na half-cell beginning from the OCV for the estimation of the sodium-ion chemical diffusion coefficient (D_{Na}) based on previous numeral assumptions and simplifications (Supplementary Note 1)[45]. The adopted measurement conditions, equations used for D_{Na} calculation, results (Supplementary Figure 9) and related discussion are provided in the Supplementary note 1. The sodium coefficient values are in range of 1.65×10^{-9} to 4.23×10^{-11} and 2.04×10^{-9} to 3.95×10^{-11} ($cm^2\ s^{-1}$) for the discharge and charge process, respectively. These obtained values are significantly higher than previous reports (10^{-12} to $10^{-16}\ cm^2\ s^{-1}$)[46,47]. It should be noted that the diffusion coefficient calculation from GITT data is decidedly determined by material nature properties (atomic weight, specific density, molar volume) and experimental parameters (active material mass, electrode area, current pulse, current rate, relaxation time)[48]. The estimated D_{Na} value reaches their peak at around 0.35 and 2.0 V during discharge and charge process, respectively (Supplementary Figure 9d). The two different potentials at which high D_{Na} values were estimated indeed match well with the low discharge potential wherein conversion reaction is assumed to occur and with the high charge potential related to great diffusion rates, respectively, as evidenced from the CV studies.

In addition, the relatively low polysulfide dissolution and hence lesser active material loss can facilitate higher reversible charge capacities with negligent capacity fade over long-term cycling of the MnS electrode utilizing diglyme-based electrolyte medium. On the other hand, the intercalation process occurring in multi-steps at the high working potential region can provide necessary padding-steps to effectively reduce the sudden volume change along discharge depth. As shown in Fig. 4a, the DS-MnS could maintain more than 1000 cycles at a relatively high current density of $5\ A\ g^{-1}$ with a 50-cycle activation at $0.5\ A\ g^{-1}$. And a reversible capacity of ~344 $mAh\ g^{-1}$ was recorded at the 1100th cycle. An excellent rate performance was also recorded herein. Figure 4b shows a high-rated performance wherein DS-MnS could deliver average discharge capacities of 227, 284, 312, 324, 336, 354, and 380.8 $mAh\ g^{-1}$ at 20, 10, 5, 4, 3, 2, and $1.0\ A\ g^{-1}$, respectively. Moreover, when the cell returns to the second subsequent round, the discharge capacity increased slightly due to the activation phenomenon. It is interesting to note that the electrochemical performance of the present dandelion-shaped MnS electrode in the diglyme electrolyte medium is exceptionally higher than those compared to the already reported MnS electrodes in the usual carbonate-based electrolyte medium.

Considering that manganese sulfides have not been tested in diglyme-based electrolytes so far and that their electrochemical patterns are different from those in carbonate-based electrolyte medium, herein we propose a new reaction mechanism. Unlike the report for the case in carbonate-based electrolytes, the reaction mechanism for MnS in the present diglyme electrolyte system can be described by a combination of intercalation (Eq. 1) and conversion (Eq. 2) reactions during discharge cycling, whereas the charging process is mainly explained by the fast kinetic conversion reaction (Eq. 3) that leads back to the formation of pristine MnS[49]. This reversible reaction mechanism occurring in the diglyme electrolyte medium ensures the maintenance of a long and stable cycle life without any serious capacity loss. The superior performance demonstrated by the DS-MnS//$NaPF_6$/diglyme//Na battery system can be related to the use of the specific electrolyte medium. Recently, glyme-based electrolytes were demonstrated to facilitate efficient plating-stripping behavior in battery applications due to the aggressive formation of a protective layer (composed of sodium oxide and sodium fluoride) that tends to limit electrolyte solvent wetting and dendritic growth[50]. Another series of studies concluded that, upon using glyme-based electrolytes, the co-intercalation of Na-ions and solvent molecules occurred during electrochemical discharge reaction and thus resulted in the formation of ternary graphite-intercalation compounds (t-GIC) when a graphite electrode was tested[51]. More recently, Cary et al. identified the highly ordered co-intercalation of Na-ions and Na-contained glyme-based solvent or sodium-encapsulated diglyme solvent shells in electrodes of sodium-ion batteries. In specific, they demonstrated that the presence of this sodium-encapsulated diglyme shells formed a “non-stick coating” layer during electrochemical reaction. They concluded that the presence of this “non-stick coating” layer facilitated greater insertion and also mitigated desolvation kinetics at the electrode-electrolyte interface ultimately leading to exceptional cycle stabilities under even high current densities (~1–30 $A\ g^{-1}$)[52]. Similarly, the present MnS electrode in a diglyme-based electrolyte medium showed remarkable cycling stability (Fig. 4) under even high current densities (>1 $A\ g^{-1}$). Hence, it can be reasonable to conclude that the “non-stick coating” layer or sodium-encapsulated diglyme solvent shells can fully cover the active primary particles and also contribute to the electrochemical properties of the MnS electrode though further investigations are required to confirm this finding. Nevertheless, the contribution from lesser polysulfide dissolution, less active material loss in the diglyme-based electrolyte medium is significant to realize high reversible specific capacities and better performance in the present dandelion-shaped MnS electrode.

Reaction mechanism of MnS/Na half-cell through XPS analysis. Ex-situ XPS was performed for further confirmation of the proposed electrochemical mechanism. Figure 5a and b present the photoelectron spectra of the Mn 2*p* and S 2*p* species at the OCV and end conditions of the 1st and 10th cycles. According to the literature for Mn $2p_{3/2}$, the peak positions of Mn^{2+} and Mn^0 spectra were fitted at 641.4 and 638.7 eV, respectively, whereas S $2p_{3/2}$ spectrum was fitted with a doublet representing the spin-orbit splitting of S $2p_{3/2}$ at 161.8 eV and S $2p_{1/2}$ at 162.7 eV[49,53,54]. In the first discharge cycle, the Mn $2p_{3/2}$ profile is mainly resolved into two peaks, the higher energy peak of which matches with the Mn^{2+} lines of OCV and the lower energy peak stands below 641.4 eV, thereby revealing the reduction of manganese oxidation state from +2. Almost similar environments are observed at the

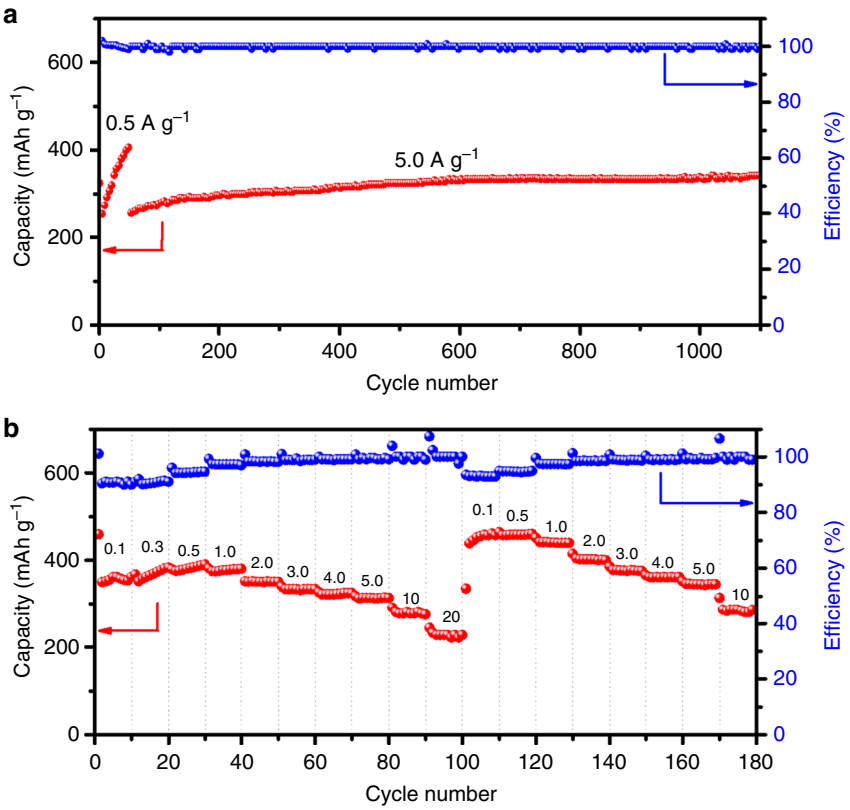

Fig. 4 Electrochemical performance of MnS/Na half-cell. **a** Cycle performance at 5.0 A g^{-1}. **b** Rate capability at different current densities from 0.3 to 20 A g^{-1}. The red and blue scatters in **a** and **b** represent obtained capacity and corresponding columbic efficiency, respectively. The index numbers in **b** are different current densities (unit A g^{-1})

first cut-off charge potential, 2.5 V, where the main peak stands at +2 state. The same trend in the manganese oxidation state is almost repeated when analyzing the 10th cycle. This evidence clearly suggests the formation of Na_xMnS (where $x < 1$) due to intercalation/conversion process during discharge process and the reformation of MnS while charging. Interestingly, there is no evidence of metallic Mn^0 lines in the ex situ XPS profile after discharge reaction which can be due to the nanosized metallic Mn being encapsulated by a layer (of the Na_2S matrix) that is sufficiently thick to prevent the penetration/detecting power of the XPS tool. This observation is supported by the finding that nanosized metallic transition metal particles grew against the compressive action of Na_2S or Li_2S shells during the discharge cycling of sulfides for LIB/SIB applications. According to these studies, upon complete discharge, the formation of a transition metal core distribution within a continuous Na_2S/Li_2S phase was proposed[55,56]. This possibility of the metallic core encapsulated by a continuous Na_2S layer during the discharge reaction supports the ex-situ TEM-results as the overall mapping image revealed an internal aggregation of Mn element (Fig. 3b) combined with the observation of a relatively increased metallic distribution at the electrode core, as evidenced by the line profiling studies (Supplementary Figure 8). In other words, these results support the proposed electrochemical mechanism reaction featuring a final phase that contains Mn metal within a continuous growth of Na_2S phase during sodiation. Alternatively, the absence of metallic Mn^0 lines in the present XPS spectrum can also be related to the easy oxidation of Mn(0) to higher states due to the high ion beam used for the XPS measurement. Although these observations seem to support the former case, more sophisticated studies are required to confirm this finding. Nevertheless, in contrast, the mainly deconvoluted peak of the S $2p_{3/2}$ species (red scatter) fluctuates around the S^{2-} reference during the charge/discharge conditions. The minor shoulder peak at the lower binding energy (~159 eV) can be related to polysulfide formation (central/terminal polysulfide) on the surface of the loaded electrode sample[57,58]. Additionally, the incompleteness of the conversion reaction (Eq. 3) during charging could lead to the formation of an intermediate-phase Mn_yS_z, which matches well with the monosulfide (S_2^{2-}) species at 162.5 eV[59].

The formation of a SEI layer when using the $NaPF_6$/diglyme electrolyte is expected to be a major factor determining the DS-MnS electrochemical enhancement. Therefore, XPS was performed to investigate possible species in the SEI layer. Figure 5c illustrates the C 1*s*, O 1*s*, Na 1*s*, and F 1*s* spectra of the first discharge state (0 V). The fitted peaks of the C 1*s* spectrum were indexed with binding energies of 284.8 eV (C–C, C–H) and 288.2 eV (C–O). Meanwhile, the O 1*s* spectrum was fitted by two peaks at 531.3 eV (Na–O) and 536.2 eV (C–O). Furthermore, the peaks of Na 1s and F 1*s* were assigned to 1071.5 eV (Na–O or Na–F), 687.3 eV (P–F) and 684.4 eV (Na–F), respectively. These observations on the abovementioned species were consistent with those of the reduction products of the $NaPF_6$/diglyme electrolytes (Supplementary Table 1)[50]. Thus it is reasonable to conclude that the mixture of RCH_2O–Na, Na_2O, NaF, Na_xPF_y, and $Na_xPO_yF_z$ tends to form a stable protective layer. The mechanical strength of the SEI protective layer was investigated by performing the depth profile study of the initially discharged sample, combining a sequence of ion-gun etching cycles interleaved with XPS measurement from the surface. Supplementary Figure 10 shows the XPS patterns of C 1*s*, O 1*s*, Na 1*s* and F 1*s* spectra after 5-min depth profiling. Although the surface of the electrode sample was etched under a high energy beam for long duration, the main XPS peaks of the functional species in the SEI layer are still

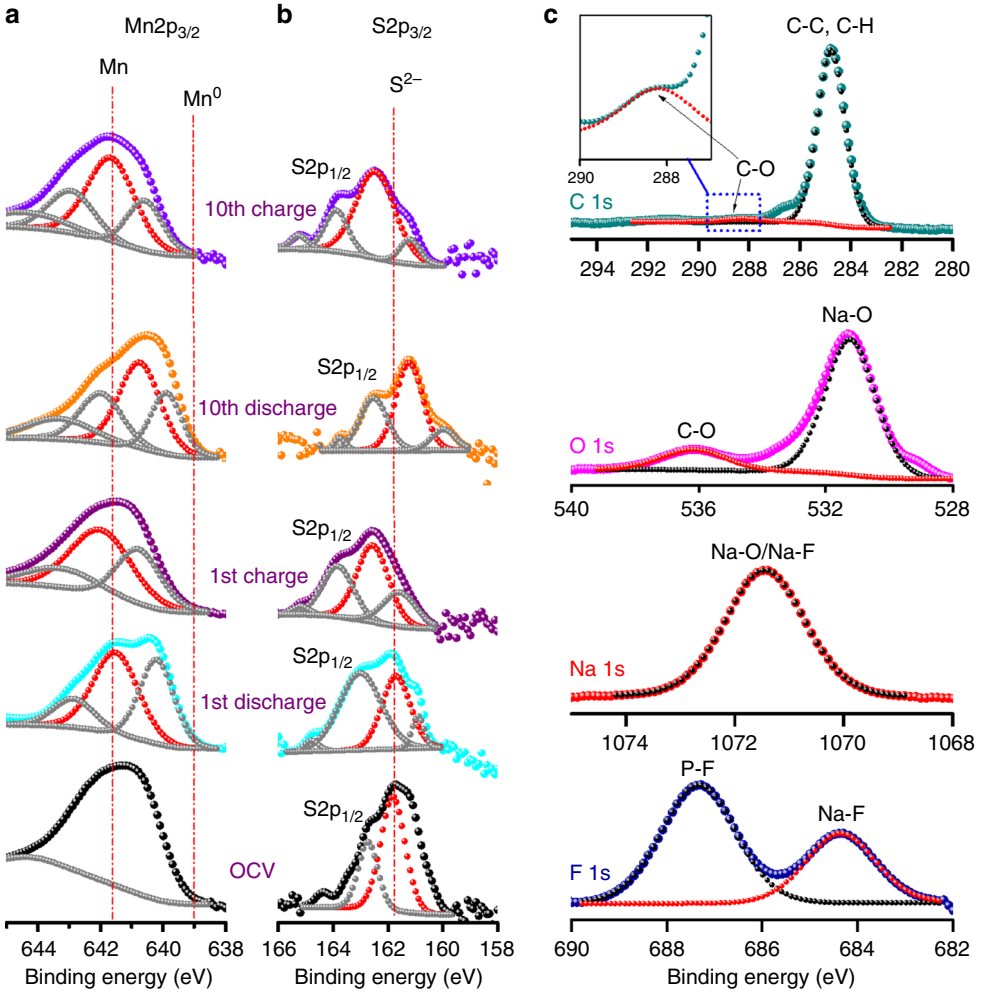

Fig. 5 Ex-situ XPS investigation. **a** and **b** XPS profile variations of Mn 2*p* and S 2*p* species after discharge/charge conditions of the 1st and 10th cycle. The red dot lines at 641.4, 638.7, and 161.8 eV represent to Mn^{2+} $2p_{3/2}$, Mn^0 $2p_{3/2}$, and S^{2-} $2p_{3/2}$ references, respectively. The colored curves in **a** and **b** are obtained XPS profiles. The red and gray scatters in **a** and **b** are major and minor deconvoluted peaks, respectively. **c** Characterization of the SEI formed using 1 M $NaPF_6$ in diglyme by C 1s, O 1s, Na 1s, and F 1s spectra at the end of first discharge. The insert of **c**: enlarge image (blue box) of C–O bond in C 1s spectrum. The red and black scatters in **c** are deconvoluted peaks

detectable, stable and of high intensities, indicating the excellent mechanical strength and high coverage of the protective layer.

SEI layer evolution and Na-ion diffusion kinetic through in situ PEIS measurement. The formation of a stable SEI layer is considered as being highly protective of the active material when the diglyme electrolyte is used[16,26,28,33]. An in situ PEIS was conducted during the galvanostatic charge/discharge process to approach this issue from a different perspective. The Nyquist-plots resulting from PEIS measurements between 10 mHz and 1 MHz at different potentials of interest, namely, 2.5, 1.5, 0.5, and 0 V (discharge) and 1.0, 2.0, and 2.5 V (charge) were carefully examined. Figure 6 presents the EIS behavior of the DS-MnS/Na coin cell in the 1st (a), 2nd (b), and subsequent (c) cycles. In the first discharge in Fig. 6a, a small semicircle in a high–medium-frequency (H–MF) region with a large arc in the low-frequency (LF) region is representative of the OCV state, which also illustrated a large charge-transfer resistance coupled with a double capacitance. The semicircle slightly shifted in their magnitudes (~80 ohm at 0 V) during discharge depths, because of the blocking effect of the inactive electrode. However, the angle of the inclined line in the LF region was dramatically reduced because of the solid-state diffusion process. In the fully charged state at 2.5 V, the semicircle resistance gradually decreased to 31 ohms. In the second cycle (Fig. 6b), a remarkable difference in EIS behavior was observed between the high and low working potentials, which clearly is demonstrated by a complex reaction mechanism. Similar EIS patterns observed for 0.5 and 0 V in the second discharge, which is an almost similar trend in the 1st cycle, might illustrate that the dandelion-shape morphology and the Na_2S formation is limited within the outermost primary particles. Figure 6c depicts the EIS spectra after an activation of 25 cycles; the end discharging condition (0 V) curve exhibited a significant difference from those at the other investigated potentials. Thanks to the huge available room for sodium insertion, the EIS spectra of 1.5 and 0.5 V are almost the same with that plotted for 2.5 V. The diffusion of Na^+ at the lower working potential of 0.5–0 V could not easily occur because of the counter migration of S^{2-} to form Na_2S on the surface of the MnS particle[14,56]. The dominating growth of Na_2S layer hence greatly impacts the sodium-ion diffusion inside the bulk phase, which raises the H-MF semicircle resistance for 0 V to four times higher than the others.

The electrical equivalent circuit (EEC) was then fitted using a ZVIEW software to obtain the closest analog description of the electrochemical reaction in Fig. 6d. As shown in the case of the

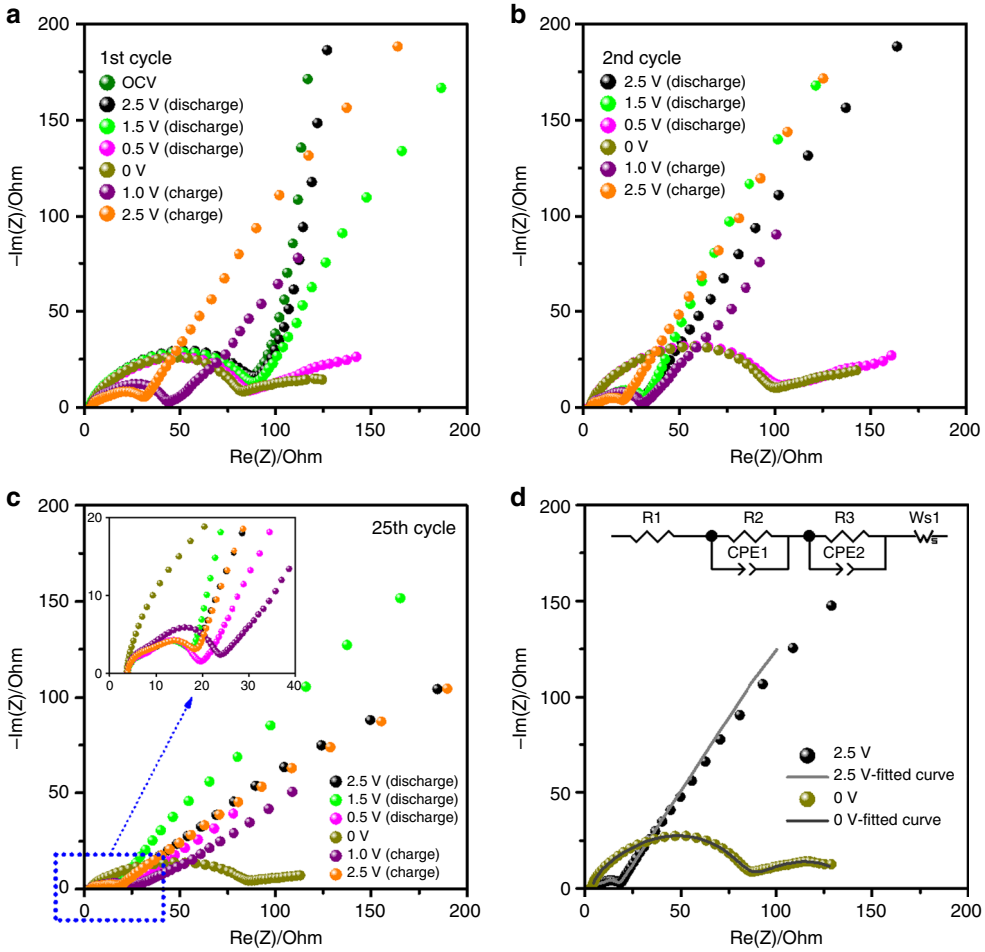

Fig. 6 In situ PEIS measurements during galvanostatic cycling. **a**–**c** Nyquist-plots of the 1st, 2nd and 25th cycle. The insert of **c** is magnified view area (blue box). **d** Fitting curves (gray lines) and equivalent circuit at the end of charge and discharge states

2.5 and 0 V EIS spectra, the fitting results matched well with the experimental plot. Based on the model of Barsoukov et al.[60], the electrochemical kinetics of the battery material can be proposed in terms of these consecutive steps: (i) ionic charge transfers through the electrolyte as well as protective separator, followed by penetration into the electrode surface; (ii) diffusion through the surface of the passivating layer (SEI) around an active material particle; (iii) charge transfer during electrochemical reaction at the interlayer of the active material and SEI layer; (iv) ionic diffusion inside the solid phase; and (v) phase transfer caused by new phase formation that corresponds to capacitive behavior and is represented by a straight line perpendicular to the Z' axis in the Nyquist plot. The EEC contains the R_1 resistor in a series connection with two parallel groups (R_2-CPE_1 and R_3-CPE_2), and is finally connected to the Warburg component, W_s. A resistance–capacitance (R–C) circuit signifies one semicircle in the Nyquist-plots of EIS that was assigned to a specific physical feature of (ii) or (iii). The CPE is a constant phase element that is practically used to replace the capacitor C. The detailed values of the EEC components of the 25th cycle were carefully analyzed and listed in Supplementary Table 2, revealing a stable SEI layer ascribed to the R_2-CPE_1 group. The resistor R_2 greatly fluctuated during the Na^+ insertion process, especially at a low working potential when the passive layer was vigorously formed by diglyme reduction, as even discussed in the XPS studies. Fortunately, this protective layer helped limit the dissolution of the polysulfide S_n^{-2} species into the electrolyte. In addition, it also aggressively controlled the development of Na_2S along the MnS particle surface. In the abovementioned activation period, the chemical grinding effect of the phase separation reaction (Eq. 2) gradually breaks down the DS-MnS particle into nanosized seeds particles. Similar material breakdown phenomena occurred in the carbonate-based electrolyte systems, which seriously affected the electrode mechanical strength[61,62]. Owing to an enduring protective layer, $NaPF_6$/diglyme could serve as a welding agent to preserve the electrode material mass during sodium-ion exchange. Supplementary Figure 11a illustrates the strong development of interface layer resistance (R_2) during activation cycling process, and reduction of charge-transfer resistance (R_3) is noted at the end of discharge state (Supplementary Figure 11b). Therefore, the Na^+ diffusion kinetics in the boundary between the SEI layer and the material surface could be markedly enhanced. Meanwhile, the other components (R_1, W_R) are maintained steadily along cycling at both charge/discharge conditions (Supplementary Figures 11c and d). The difference of W_r between end of charge and discharge states suggested an interesting ionic diffusion capability inside bulk phase of MnS. Furthermore, the diffusion coefficient (D) value could be determined by the behavior of the "straight line" at low-frequency range. This D parameter value can be calculated by following equation:

$$D = 0.5(RT/An^2F^2C\sigma)^2 \quad (4)$$

where D is the diffusion coefficient ($cm^2\ s^{-1}$); R is the gas constant; T is the absolute temperature; A is the surface area of

the anode (cm^2); n is the number of electron transfer; F is the Faraday constant; C is the ion concentration; and σ is the Warburg factor. According to Eq. (5), σ can be determined by the slope of impedance versus the $\omega^{-1/2}$ plot (Supplementary Figure 12a–f)[63,64].

$$Z_{re} = R_D + R_L + \sigma\omega^{-1/2} \quad (5)$$

The slope b-values was obtained for the individually charge/discharge potentials for the 25th cycle. This value inversely reflected the diffusion ability of sodium ions inside the bulk phase of a MnS particle. During the discharge process, the b-value gradually reduced from 70.5 to 10.7 as the sodium-ion started penetrating through the stable SEI layer into the MnS species under the influence of the driving reaction in Eq. (1). At a low working potential, the diffusion ability is restrained because of the inert Na_2S layer at the interface, produced based on the reaction attributed to Eq. (2). Interestingly, the slope value of 70.4 is achieved at the end of charge process, thereby illuminating the reversible mechanism suggested here.

Faradaic/non-Faradaic charge storage distribution mechanism. Another analysis based on cyclic voltammetry was performed to understand the effect of capacitive distribution on electrochemical performance. Figure 7a shows the typical CV curves for different sweep rates. The area under the curve represents a combination of faradaic and double-layer non-faradic charge storage mechanisms. Furthermore, the faradaic mechanism could be separated into two other behaviors: (i) Na^+ ion insertion and (ii) charge transfer involving the surface particles, so-called 'pseudocapacitance'[65]. The capacitive term was then used to imply all the surface charge storage effects that included both the double layer and pseudocapacitance charges. Using the power law relationship between the current i and sweep rates in Eq. (6), the capacitive distribution can be estimated by the b-value determined from the linear slope of log i vs log v.

$$i = av^b \quad (6)$$

According to the literature, the two fixed conditions of the b-value are 0.5 and 1.0, which are representative of diffusion-controlled and capacitive response, respectively[65,66]. Figure 7b shows the plot of the adjustable b parameter at several peak potential positions. The reduction peak potentials of 1.9 and 0.5 V had a b-value of ~0.8, indicating that the current was partially dominated by the capacitive behavior. While $b = 0.76$ at the oxidation peak of 2.0 V is likely favorable with the diffusion of sodium ions, this observation being congruent with the galvanostatic analysis.

Dunn et al.[66] developed an effective calculation method to provide a further examination, qualify capacitive and diffusion-controlled contributions, and quantify their values in the overall current. Based on the earlier discussion, the current response could be separated into surface capacitive (k_1v) and diffusion-controlled ($k_2v^{1/2}$) effects represented by the following equation:

$$i(V) = k_1v + k_2v^{1/2} \quad (7)$$

The equation can be simplified as a first-order equation type:

$$i(V)/v^{1/2} = k_1v^{1/2} + k_2 \quad (8)$$

By plotting the square root of the sweep rate dependence on current, k_1 and k_2 can be determined from the slope and y-axis intercept. The individual cathodic/anodic scan potential can be used to determine the k_1 and k_2 values. The $k_1v^{1/2}$ term enables us to clarify the capacitive current contribution along with the working potential range. The inset of Fig. 7c presents examples of the linear relationship of $v^{1/2}$ (x-axis) and $(i/v)^{1/2}$ (y-axis). At a given selected potential, k_1 and k_2 could be determined from the slope and y-axis intercept point of the linear line, respectively. Following the calculation, the capacitive distribution data were collected in all potential ranges and plotted in Fig. 7c for 0.5 mV s^{-1} sweep rate (red shaded). The comparison of the shaded area with the overall stored charge showed 66%, 71%, 76%, and 89% capacitive distributions in 0.5, 1.0, 2.0, and 5 mV s^{-1} scan rates, respectively (Fig. 7d).

Full-cell devices. A sodium-ion full-cell with dandelion MnS as the anode and a $Na_3V_2(PO_4)_3$@C (NVP@C) composite as the cathode was also studied herein. Before the full-cell analysis, the NVP@C cathode was optimized in sodium half-cell configuration using a diglyme-based electrolyte (1 M $NaPF_6$ in DGM) and the detailed electrochemical results are provided in Supplementary Figures 13a and b. Unlike the results of a previous report using commercial EC/DMC (1:1)-based electrolyte[67], the performance of NVP@C is inferior due to the high viscosity of the diglyme-based electrolyte. Reversible capacities of approximately 95, 90, 87 and 82 mAh g^{-1} were achieved at 50, 100, 200 and 500 mA g^{-1} current densities, respectively. The optimized mass ratio with best performance was determined to be 1:4 for MnS:NVP@C, respectively. The initial charge/discharge profile of the sodium full-cell reveals that almost 60 and 75 mAh g^{-1} discharge and charge capacities, respectively, are attained at 50 mA g^{-1} current density (Fig. 8). A highly stable cycle life was maintained for 200 cycles (a high discharge capacity of 70 mAh g^{-1}) without any capacity fading (Fig. 8b). It is worth noting that the limitation of the cathode-side capacity has decidedly affected the final results of the full-cell. However, the relatively good performance of the dandelion MnS in full-cell configurations, clearly demonstrates their feasibility for practical uses.

Overall, the ex-situ XPS, PIES and CV studies confirm the proposed electrochemical reaction mechanism proposed herein for the DS-MnS electrode in the diglyme-based electrolyte medium. In short, the ex-situ XPS studies suggests the formation of a Na_xMnS (intermediate phase)/polysulfide phase in addition to the formation of a highly protective SEI layer along the surface of the primary seed particle in the secondary MnS electrode during electrochemical discharge cycling. PIES studies support the notion that the protective SEI layer tends to limit the dissolution of the polysulfide species into the electrolyte and thereby preserve the active electrode material on continuous discharge/charge cycling. The analysis of the derived modelling circuit revealed that the Na^+ diffusion in the bulk is limited at low discharge potentials due to the competing growth of the polysulfide layer along the particle boundary and also confirmed that the proposed electrochemical reaction is reversible, as evidenced form the diffusion coefficients determined at various states of cycling discharge/charge potentials. Also, this study suggested that the Na^+ diffusion at the SEI/active material interface tends to increase on repeated cycling. CV studies reinforced that the present DS-MnS electrode demonstrates capacitive storage behavior low discharge potentials that also contributed to the overall specific capacity of the electrode. Therefore, the present study clearly indicates that the secondary DS-MnS electrode employed in a combination with a diglyme-based electrolyte is attractive for high energy SIB applications.

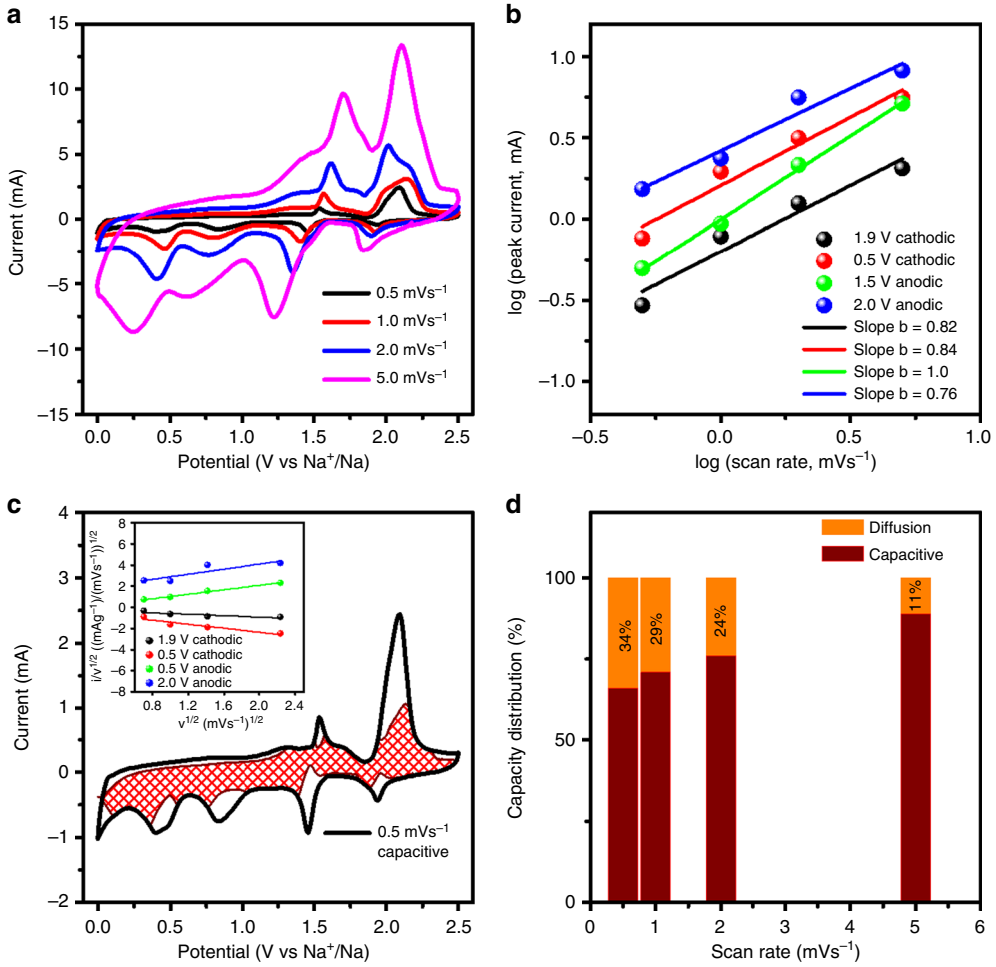

Fig. 7 Capacitive charge storage distribution calculation. **a** CV curves at different scan rates. **b** Power law ($i = av^b$) dependence of current on sweep rate for obtaining *b*-values at peak currents. **c** CV curves with separation between total current (solid line) and surface (shaded regions) at 0.5 mV s^{-1}. The insert of **c**: use of Eq. (8) to analyze the CV data at different sweep rates from 0.5 to 5 mV s^{-1}. **d** Comparison of the capacitive and diffusion capacities distribution

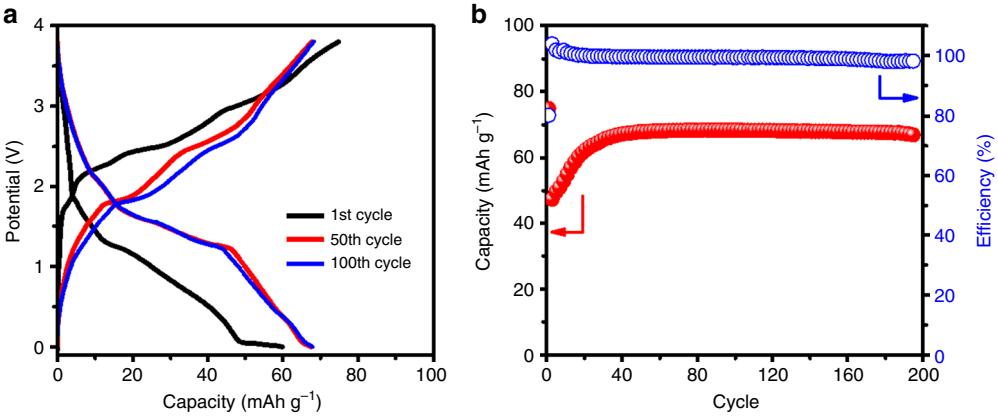

Fig. 8 Sodium-ion full-cell $Na_3V_2(PO_4)_3$@C–MnS electrochemical performance. **a** Charge-discharge curves at 50 mA g^{-1} in the voltage range of 0–3.8 V. **b** Cycle performance. The red and blue scatters in **b** represent obtained capacity and corresponding columbic efficiency, respectively

Furthermore, this study also demonstrated that the drawbacks related to the electrochemical properties of transition metal sulfides for battery applications could be overcome by applying suitable strategies for material synthesis and making the appropriate choice of electrolyte components.

Discussion

The dandelion-shaped MnS secondary electrode composed of nanosized primary seeds was successfully prepared by a single-step solvothermal method. Moreover, the high compatibility of the $NaPF_6$/diglyme electrolyte confirmed its role as a crucial agent

that helps to overcome the issue of polysulfides dissolution in normal carbonate electrolytes. Owing to the high mechanical strength of the protective layer that was generated during the activation period, the material mass was preserved during sodium-ion exchange. Hence DS-MnS could easily retain the capacity of ~340 mAh g^{-1} at 5.0 A g^{-1} for more than 1000 cycles without any fading. Furthermore, the analysis of a MnS//$NaPF_6$-diglyme//$Na_3V_2(PO_4)_3$@C full-cell configuration demonstrated its excellent cycle life, thus opening the prospects for MnS anode to be utilized in real-time SIB applications. Moreover, a durable "non-stick" coating at material interface along with large reaction sites, derived from nanosized activated species during discharge/charge processes, provide an excellent rate performance, high capacity, and long cycle life of DS-MnS. In addition, our study also reviewed the impact of parasitic/side reactions to MnS electrode at low-rate performance as the most common issue of anode materials with high surface area, which could be easily avoided at high rates. Furthermore, a detailed reaction mechanism carefully revealed the combination of Na^+ intercalation and conversion behaviors in discharge and fast kinetic conversion in charge process. New study approaches based on PEIS and capacitive distribution calculations were also included, providing a different perspective of the electrochemical performance of DS-MnS for SIBs.

Methods

Materials. The DS-MnS was synthesized by a facile one-step solvothermal method. 4 mmol of manganese acetate tetra-hydrate $(CH_3COO)_2$ Mn·$4H_2O$ was homogenously mixed in 30 ml ethylene glycol (EG). In addition, 8 mmol $NaBH_4$ was separately dispersed in 30 ml EG, followed by the addition of 8 mmol S powder. These solutions were slowly mixed under continuous stirring for 2 h. The mixture was then kept in a hot sonication bath (80 °C) for 30 min, after which the mixture was loaded into a Teflon-lined autoclave with a seal and maintained at 200 °C for 12 h in a high-temperature conventional oven. Dark-green precipitates were formed and washed several times with ethanol and acetone. Finally, the obtained product was dried overnight in an oven at 80 °C.

Characterization. Structural characterization of the powder was performed using a synchrotron powder X-ray diffractometer from the 8C station beamline of the Pohang light source (South Korea). The diffraction data were obtained in the 2θ scanning angle range 10°–80° with 0.01° steps. The structural morphology and lattice fringe were examined by field emission scanning electron microscopy (FE-SEM, S4700 Hitachi) and high resolution transmission electron microscopy (HR-TEM, Philips Tecnai F20 at 200 kV), respectively.

Electrochemical measurements. A half-cell CR2032 was assembled using a MnS electrode with sodium metal as the counter and reference electrode, and 1 M $NaPF_6$ in diglyme (DGM) was used as electrolyte. The working electrodes were prepared by mixing the active material (80%), Super P (10%), 5 wt.% aqueous solution of sodium carboxymethyl cellulose (4%), and 50 wt.% aqueous solution of styrene-butadiene rubber (6%). An optimized amount of distilled water was added to the mixture and mixed in a Spex ball mill for 10 min to obtain a homogeneous slurry, which was then uniformly coated onto a copper foil (battery grade) current collector. The electrode mass loading was tuned at 1.5 mg cm^{-2}. The MnS half-cell measurements were performed within the potential range of 0 to 2.5 V (vs. Na/Na^+) at different current densities. Galvanostatic studies and cyclic voltammetry (CV) were performed on the coin cell type assembled in an argon-filled glove box using a programmable battery tester (BTS–2004H, Nagano, Japan and Bio-Logic Science Instruments).

The full-cell sodium-ion battery was constructed using MnS as anode and $Na_3V_2(PO_4)_3$@C (NVP@C) as cathode in a CR2032-type coin cell. The cathode material was prepared on the basis of our earlier report[68]. The active material was mixed with Ketjen black (Lion Corporation, Japan) as conducting agent and commercial available teflonized acetylene black (TAB, Hohsen Corporation, Japan) as the binder in a ratio of 80:10:20 and pressed on stainless steel mesh. The calculated and optimized weight ratio between the two electrodes was 1: 4 (anode: cathode). The electrolyte was 1 M $NaPF_6$ in DGM with a separator (Whatman). The full cells operated in the voltage range of 0–3.8 V at a current density of 50 mA g^{-1}.

Ex-situ XPS. Ex-situ samples were prepared using MnS half-cell, loading under 0.3 A g^{-1} current density. At each cut-off potential, the cell was hold for 1 h to reach equilibrium. After that, the loaded cells were disassembled in an argon-filled glove box to obtain the ex-situ electrodes, which were then thoroughly washed in diglyme. The oxidation states of the electrode sample were determined by XPS (Thermo VG Scientific Instrument, Multilab 2000) using Al K_α as the X-ray source. The spectrometer was calibrated at 284.8 eV corresponding to the C 1*s* peak binding energy.

In situ PEIS. The real-time Galvanostatic-impedance measurement was conducted by Bio-logic Science Instrument using MnS half-cell. The sample was loaded under the current pulse of 0.3 A g^{-1}. Along discharge/charge loading, the investigated points were hold at specific potentials for EIS measurements. The frequency range was set in range of 10 mHz–1 Mhz.

GITT analyses. The GITT experiment is performed in the voltage range 0–2.5 V of the first discharge/charge cycle. Firstly, the cell is discharged from OCV at a $\tau = 5$ min current pulse of 0.1 A g^{-1}, followed by 40 min relaxation time to allow the system to reach the electrochemical equilibrium status. This process is followed for the entire working potential window.

Data availability

The data that support the findings of this study are available from the corresponding authors upon reasonable request.

Received: 20 April 2018 Accepted: 25 October 2018
Published online: 15 November 2018

References

1. Kim, T. H. et al. The current move of lithium ion batteries towards the next phase. *Adv. Energy Mater.* **2**, 860–872 (2012).
2. Mahmood, N., Tang, T. & Hou, Y. Nanostructured anode materials for lithium ion batteries: progress, challenge and perspective. *Adv. Energy Mater.* **6**, 1600374 (2016).
3. Peng, L., Zhu, Y., Chen, D., Ruoff, R. S. & Yu, G. Two-dimensional materials for beyond-lithium-ion batteries. *Adv. Energy Mater.* **6**, 1600025 (2016).
4. Vaalma, C., Buchholz, D., Weil, M. & Passerini, S. A cost and resource analysis of sodium-ion batteries. *Nat. Rev. Mater.* **3**, 18013 (2018).
5. Yabuuchi, N., Kubota, K., Dahbi, M. & Komaba, S. Research development on sodium-ion batteries. *Chem. Rev.* **114**, 11636–11682 (2014).
6. Rojo, T., Hu, Y.-S., Forsyth, M. & Li, X. Sodium-ion batteries. *Adv. Energy Mater.* **8**, 1800880 (2018).
7. Delmas, C. Sodium and sodium-ion batteries: 50 years of research. *Adv. Energy Mater.* **8**, 1703137 (2018).
8. Xu, G. L. et al. Challenges in developing electrodes, electrolytes, and diagnostics tools to understand and advance sodium-ion batteries. *Adv. Energy Mater.* **8**, 1702403 (2018).
9. Pan, H., Hu, Y. S. & Chen, L. Room-temperature stationary sodium-ion batteries for large-scale electric energy storage. *Energy Environ. Sci.* **6**, 2338–2360 (2013).
10. Yuan, Y., Amine, K., Lu, J. & Shahbazian-Yassar, R. Understanding materials challenges for rechargeable ion batteries with in situ transmission electron microscopy. *Nat. Commun.* **8**, 15806 (2017).
11. Palomares, V. et al. Na-ion batteries, recent advances and present challenges to become low cost energy storage systems. *Energy Environ. Sci.* **5**, 5884 (2012).
12. Ponrouch, A. et al. Towards high energy density sodium ion batteries through electrolyte optimization. *Energy Environ. Sci.* **6**, 2361 (2013).
13. Xiao, Y., Lee, S. H. & Sun, Y.-K. The application of metal sulfides in sodium ion batteries. *Adv. Energy Mater.* **7**, 1601329 (2017).
14. Hu, Z. et al. Pyrite FeS_2 for high-rate and long-life rechargeable sodium batteries. *Energy Environ. Sci.* **8**, 1309–1316 (2015).
15. Peng, S. et al. Unique cobalt sulfide/reduced graphene oxide composite as an anode for sodium-ion batteries with superior rate capability and long cycling stability. *Small* **12**, 1359–1368 (2016).
16. Su, D., Dou, S. & Wang, G. Ultrathin MoS_2 nanosheets as anode materials for sodium-ion batteries with superior performance. *Adv. Energy Mater.* **5**, 1–6 (2015).
17. Li, J. et al. Significantly improved sodium-ion storage performance of CuS nanosheets anchored into reduced graphene oxide with ether-based electrolyte. *ACS Appl. Mater. Interfaces* **9**, 2309–2316 (2017).
18. Kim, J. S. et al. The electrochemical properties of copper sulfide as cathode material for rechargeable sodium cell at room temperature. *J. Power Sources* **189**, 864–868 (2009).
19. Chevrier, V. L. & Ceder, G. Challenges for Na-ion negative electrodes. *J. Electrochem. Soc.* **158**, A1011–A1014 (2011).

20. Zhang, S. S. & Tran, D. T. Mechanism and solution for the capacity fading of Li/FeS_2 battery. *J. Electrochem. Soc.* **163**, A792–A797 (2016).
21. Xu, X. et al. Lithium reaction mechanism and high rate capability of VS_4-graphene nanocomposite as an anode material for lithium batteries. *J. Mater. Chem. A* **2**, 10847–10853 (2014).
22. Yu, H., Yang, J., Geng, H. & Li, C. C. Facile preparation of carbon wrapped copper telluride nanowires as high performance anodes for sodium and lithium ion batteries. *Nanotechnology* **28**, 145403 (2017).
23. Xue, H. et al. Pyrite FeS_2 microspheres wrapped by reduced graphene oxide as high-performance lithium-ion battery anodes. *J. Mater. Chem. A* **3**, 7945–7949 (2015).
24. Gümüş, C., Ulutaş, C. & Ufuktepe, Y. Optical and structural properties of manganese sulfide thin films. *Opt. Mater. (Amst.).* **29**, 1183–1187 (2007).
25. Tang, Y., Chen, T. & Yu, S. Morphology controlled synthesis of monodispersed manganese sulfide nanocrystals and their primary application in supercapacitors with high performances. *Chem. Commun.* **51**, 9018–9021 (2015).
26. Zhang, N. et al. Hydrothermal synthesis and electrochemical properties of alpha-manganese sulfide submicrocrystals as an attractive electrode material for lithium-ion batteries. *Mater. Chem. Phys.* **111**, 13–16 (2008).
27. Ma, D., Huang, S. & Zhang, L. One-pot synthesis and magnetic, electrical properties of single-crystalline α-MnS nanobelts. *Chem. Phys. Lett.* **462**, 96–99 (2008).
28. Ha, D. H. et al. A general method for high-performance li-ion battery electrodes from colloidal nanoparticles without the introduction of binders or conductive-carbon additives: the cases of MnS, $Cu_{2-x}S$, and Ge. *ACS Appl. Mater. Interfaces* **7**, 25053–25060 (2015).
29. Xu, X., Ji, S., Gu, M. & Liu, J. In situ synthesis of MnS hollow microspheres on reduced graphene oxide sheets as high-capacity and long-life anodes for Li- and Na-ion batteries. *ACS Appl. Mater. Interfaces* **7**, 20957–20964 (2015).
30. Lalancette, J. M., Frêche, A., Brindle, J. R. & Laliberté, M. Reductions of functional groups with sulfurated borohydrides. application to steroidal ketones. *Synthesis* **10**, 526–532 (1972).
31. Wang, D.-W., Wang, Q.-H. & Wang, T.-M. Controlled growth of pyrite FeS_2 crystallites by a facile surfactant-assisted solvothermal method. *CrystEngComm* **12**, 755–761 (2010).
32. Feng, S. & Guanghua, L. (eds). *Modern Inorganic Synthetic Chemistry* 2nd edn, 73–104 (Elsevier, North-Holland, 2017).
33. Liu, Y. et al. Coral-like α-MnS composites with N-doped carbon as anode materials for high-performance lithium-ion batteries. *J. Mater. Chem.* **22**, 24026–24033 (2012).
34. Ding, S., Zhang, D., Chen, J. S. & Lou, X. W. Facile synthesis of hierarchical MoS_2 microspheres composed of few-layered nanosheets and their lithium storage properties. *Nanoscale* **4**, 95–98 (2012).
35. Chang, K. & Chen, W. L-cysteine-assisted synthesis of layered MoS_2/graphene composites with excellent electrochemical performances for lithium ion batteries. *ACS Nano* **5**, 4720–4728 (2011).
36. Sun, R. et al. Novel layer-by-layer stacked VS_2 nanosheets with intercalation pseudocapacitance for high-rate sodium ion charge storage. *Nano Energy* **35**, 396–404 (2017).
37. Chu, C. et al. Biphase-interface enhanced sodium storage and accelerated charge transfer: flower-like anatase/bronze TiO_2/C as an advanced anode material for Na-ion batteries. *ACS Appl. Mater. Interfaces* **9**, 43648–43656 (2017).
38. Li, Z., Wang, Y. F., Wang, X. W., Yang, Z. & Zeng, J. H. Doping as an effective recombination suppressing strategy for performance enhanced quantum dots sensitized solar cells. *Mater. Lett.* **221**, 42–45 (2018).
39. Lodovico, L., Varzi, A. & Passerini, S. Radical decomposition of ether-based electrolytes for Li-S batteries. *J. Electrochem. Soc.* **164**, A1812–A1819 (2017).
40. Xu, D. et al. l-cysteine-assisted synthesis of urchin-Like γ-MnS and its lithium storage properties. *Nanoscale Res. Lett.* **11**, 444 (2016).
41. Jin, P., Zhang, X. & Wang, J. Mesoporous γ-MnS nanospheres as anode materials for Li ion batteries. *Mater. Lett.* **188**, 13–16 (2017).
42. Wang, L. P., Yu, L., Wang, X., Srinivasan, M. & Xu, Z. J. Recent developments in electrode materials for sodium-ion batteries. *J. Mater. Chem. A* **3**, 9353–9378 (2015).
43. Jache, B., Mogwitz, B., Klein, F. & Adelhelm, P. Copper sulfides for rechargeable lithium batteries: Linking cycling stability to electrolyte composition. *J. Power Sources* **247**, 703–711 (2014).
44. Yim, T. et al. Effect of chemical reactivity of polysulfide toward carbonate-based electrolyte on the electrochemical performance of Li-S batteries. *Electrochim. Acta* **107**, 454–460 (2013).
45. Weppner, W. Determination of the kinetic parameters of mixed-conducting electrodes and application to the system Li_3Sb. *J. Electrochem. Soc.* **124**, 1569 (1977).
46. Guo, S. et al. Understanding sodium-ion diffusion in layered P2 and P3 oxides via experiments and first-principles calculations: A bridge between crystal structure and electrochemical performance. *NPG Asia Mater.* **8**, e266 (2016).
47. Cao, Y. et al. Reversible sodium ion insertion in single crystalline manganese oxide nanowires with long cycle life. *Adv. Mater.* **23**, 3155–3160 (2011).
48. West, K., Jacobsen, T., Zachau-Christiansen, B. & Atlung, S. Determination of the differential capacity of intercalation electrode materials by slow potential scans. *Electrochim. Acta* **28**, 97–107 (1983).
49. Tan, R. et al. Core–shell nano-FeS_2@N-doped graphene as an advanced cathode material for rechargeable Li-ion batteries. *Chem. Commun.* **52**, 986–989 (2016).
50. Seh, Z. W., Sun, J., Sun, Y. & Cui, Y. A highly reversible room-temperature sodium metal anode. *ACS Cent. Sci.* **1**, 449–455 (2015).
51. Jache, B. & Adelhelm, P. Use of graphite as a highly reversible electrode with superior cycle life for sodium-ion batteries by making use of co-intercalation phenomena. *Angew. Chem. Int. Ed.* **53**, 10169–10173 (2014).
52. Cohn, A. P., Share, K., Carter, R., Oakes, L. & Pint, C. L. Ultrafast solvent-assisted sodium ion intercalation into highly crystalline few-layered graphene. *Nano Lett.* **16**, 543–548 (2016).
53. Nesbitt, H. W. & Banerjee, D. Interpretation of XPS Mn(2p) spectra of Mn oxyhydroxides and constraints on the mechanism of MnO_2 precipitation. *Am. Mineral.* **83**, 305–315 (1998).
54. Wang, T. X. & Chen, W. W. Low-temperature synthesis of pure rock-salt structure manganese sulfide using a single-source molecular precursor. *Chem. Eng. J.* **144**, 146–148 (2008).
55. Boebinger, M. G. et al. Distinct nanoscale reaction pathways in a sulfide material for sodium and lithium batteries. *J. Mater. Chem. A* **5**, 11701–11709 (2017).
56. Yamakawa, N., Jiang, M. & Grey, C. P. Investigation of the conversion reaction mechanisms for binary Copper(II) compounds by solid-state NMR spectroscopy and X-ray diffraction. *Chem. Mater.* **21**, 3162–3176 (2009).
57. Liang, X. et al. A highly efficient polysulfide mediator for lithium-sulfur batteries. *Nat. Commun.* **6**, 5682 (2015).
58. Fantauzzi, M., Elsener, B., Atzei, D., Rigoldi, A. & Rossi, A. Exploiting XPS for the identification of sulfides and polysulfides. *RSC Adv.* **5**, 75953–75963 (2015).
59. Pratt, A., Muir, I. & Nesbitt, H. X-ray photoelectron and Auger electron spectroscopic studies of pyrrhotite and mechanism of air oxidation. *Geochim. Cosmochim. Acta* **58**, 827–841 (1994).
60. Barsoukov, E. & Macdonald, J. R. *Impedance Spectroscopy: Theory, Experiment, and Applications. Impedance Spectroscopy: Theory, Experiment, and Applications.* (John Wiley & Sons, Inc, Hoboken, NJ, 2005).
61. Chen, D., Quan, H., Huang, Z. & Guo, L. Mesoporous manganese sulfide spheres anchored on graphene sheets as high-capacity and long-life anode materials for lithium-ion batteries. *ChemElectroChem* **2**, 1314–1320 (2015).
62. Hao, Y. et al. Studies on intrinsic phase-dependent electrochemical properties of MnS nanocrystals as anodes for lithium-ion batteries. *J. Power Sources* **338**, 9–16 (2017).
63. Chou, S. L., Wang, J. Z., Liu, H. K. & Dou, S. X. Rapid synthesis of $Li_4Ti_5O_{12}$ microspheres as anode materials and its binder effect for lithium-ion battery. *J. Phys. Chem. C* **115**, 16220–16227 (2011).
64. Shi, Y. et al. Hollow structured Li_3VO_4 wrapped with graphene nanosheets in situ prepared by a one-pot template-free method as an anode for lithium-ion batteries. *Nano Lett.* **13**, 4715–4720 (2013).
65. Conway, B. E., Birss, V. & Wojtowicz, J. The role and utilization of pseudocapacitance for energy storage by supercapacitors. *J. Power Sources* **66**, 1–14 (1997).
66. Wang, J., Polleux, J., Lim, J. & Dunn, B. Pseudocapacitive contributions to electrochemical energy storage in TiO_2 (Anatase) nanoparticles. *J. Phys. Chem. C* **111**, 14925–14931 (2007).
67. Song, J. et al. An enhanced high-rate $Na_3V_2(PO_4)_3$-Ni_2P nanocomposite cathode with stable lifetime for sodium-ion batteries. *ACS Appl. Mater. Interfaces* **8**, 35235–35242 (2016).
68. Islam, S. et al. A promising carbon-wrapped sponge-like $Na_3V_2(PO_4)_3$@C nanoparticles cathode via pyro-synthesis with superior rate capability and long cycle life for aqueous hybrid batteries. *Chem. Sus. Chem.* **13**, 2239–2247 (2018).

Acknowledgements

This work was mainly supported by the Global Frontier Program through the Global Frontier Hybrid Interface Materials (GFHIM) of the National Research Foundation of Korea (NRF) funded by the Ministry of Science, ICT & Future Planning (2013M3A6B1078875). This work was also supported by the National Research Foundation of Korea (NRF) grant funded by the Korea government (MSIP) (2017R1A2A1A17069397).

Author contributions

J.K., Y.K.-S., K.K., and D.T.P. designed the ideal and experimental progress. D.T.P conducted the majority of the experiments. Su.K., J.J., Se.K., and S.P. carried out the ex-situ XPS, in situ PEIS, and capacitive distribution calculation. D.T.P., B.S., and V.M. co-

wrote the paper. The results and the manuscript are commented and discussed by all authors.

Additional information

Supplementary information accompanies this paper at https://doi.org/10.1038/s42004-018-0084-1.

Competing interests: The authors declare no competing interests.

Reprints and permission information is available online at http://npg.nature.com/reprintsandpermissions/

Publisher's note: Springer Nature remains neutral with regard to jurisdictional claims in published maps and institutional affiliations.